Article

Morphology of Large ZSM-5 Crystals Unraveled by Fluorescence Microscopy

Maarten B. J. Roeffaers, Rob Ameloot, Mukulesh Baruah, Hiroshi Uji-i, Metin Bulut, Gert De Cremer, Ulrich Müller, Pierre A. Jacobs, Johan Hofkens, Bert F. Sels, and Dirk E. De Vos

J. Am. Chem. Soc., **2008**, 130 (17), 5763-5772 • DOI: 10.1021/ja7113147 • Publication Date (Web): 03 April 2008

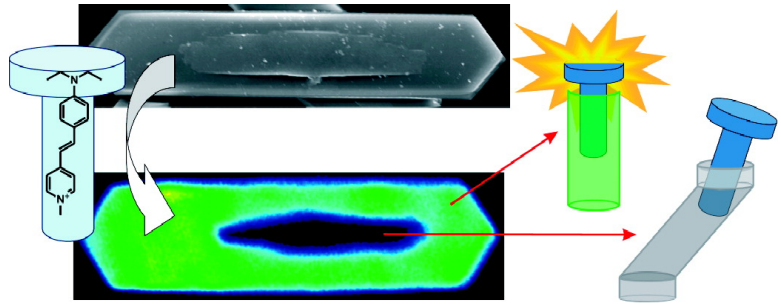

J|A|C|S
ARTICLES

Published on Web 04/03/2008

Morphology of Large ZSM-5 Crystals Unraveled by Fluorescence Microscopy

Maarten B. J. Roeffaers,[†] Rob Ameloot,[†] Mukulesh Baruah,[‡] Hiroshi Uji-i,[‡] Metin Bulut,[†] Gert De Cremer,[†] Ulrich Müller,[§] Pierre A. Jacobs,[†] Johan Hofkens,*[,‡] Bert F. Sels,[†] and Dirk E. De Vos*[,†]

Department of Microbial and Molecular Systems, Centre for Surface Chemistry and Catalysis, Katholieke Universiteit Leuven, Kasteelpark Arenberg 23, B-3001 Leuven, Belgium, Department of Chemistry, Katholieke Universiteit Leuven, Celestijnenlaan 200F, B-3001, Leuven, Belgium, and BASF AG, GCC/Z M 301, 67056 Ludwigshafen, Germany

Received December 21, 2007; E-mail: johan.hofkens@chem.kuleuven.be; dirk.devos@biw.kuleuven.be

Abstract: Understanding the internal structure of ZSM-5 crystallites is essential for improving catalyst performance. In this work, a combination of fluorescence microscopy, AFM, SEM, and optical observations is employed to study intergrowth phenomena and pore accessibility in a set of five ZSM-5 samples with different crystal morphologies. An amine-functionalized perylene dye is used to probe acid sites on the external crystal surface, while DAMPI (4-(4-diethylaminostyryl)-*N*-methylpyridinium iodide) is used to map access to the straight channels in MFI from the outer surface. The use of these dyes is validated by studying the well-understood rounded-boat type ZSM-5 crystals. Next coffin-shaped ZSM-5 crystals are considered; we critically evaluate the seemingly conflicting 2-component and 3-component models that have been proposed to account for the hourglass structure in these crystals. The data prove that observation of an hourglass structure is essentially unrelated to a 90° rotation of the pyramidal crystal components under the (010) face. Hence, in perfectly formed coffin-shaped crystals, the straight channels can be accessed from (010). However, in other crystal batches, sections with a 90° rotation can be found; they are indeed located inside the crystal sections under (010) but often only partially occupy these pyramidal components. In such a case, both straight and sinusoidal pores surface at the hexagonal face. The results largely support the 3-component model, but with the added notion that 90° rotated sections (as proposed in the 2-component model) are most likely to be formed inside the defect-rich, pyramidal crystal sections under the (010) faces.

Introduction

MFI zeolites such as ZSM-5, its all-silica analogue silicalite, and the Ti-substituted TS-1 have drawn a lot of attention because of their use in selective adsorption, separation, and catalysis. ZSM-5 is one of the most widely used zeolites, with applications as a shape-selective catalyst in the production of ethylbenzene from benzene and ethylene, in high severity fluid catalytic cracking, in xylene isomerization, in the conversion of methanol into gasoline, etc. The microporous structure of MFI materials contains straight channels (5.6 × 5.3 Å^2) along the crystallographic *b*-axis that are interconnected with sinusoidal channels (5.5 × 5.1 Å^2) along the *a*-axis. At the crystal level, ZSM-5 zeolites occur in different morphologies. Two well-recognizable forms are regularly encountered, *viz*. the rounded-boat morphology and the coffin-shaped crystals (Figure 1). In earlier work, Koegler et al. used optical and electron microscopy to illustrate that, during the crystallization of ZSM-5 crystals, the rounded-boat type crystals evolve into coffin-shaped crystals.[1] This explains why the coffin-shaped crystals, which range from a few to several hundred micrometers along the *c*-axis, are generally larger than the rounded-boat precursors, which are never larger than 20 μm.

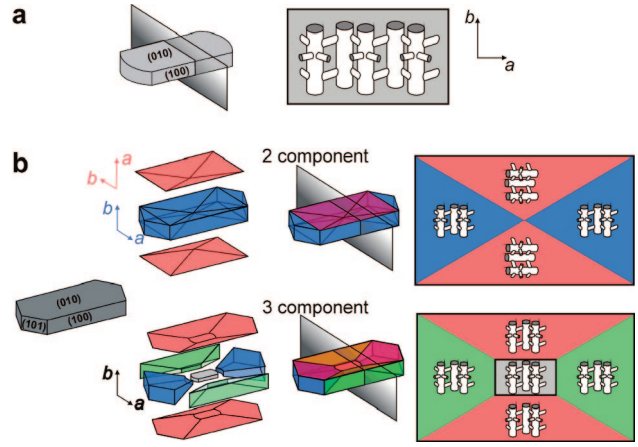

Figure 1. Schematic representation of MFI zeolite crystallography: (a) pore organization in rounded-boat crystals; (b) the 2- and 3-component models for coffin-shaped crystals.

Micrometer-sized crystals, especially of the coffin-shaped type, rarely occur as perfect single crystals. Electron micrographs often show defects at the outer surface, ranging from small ramps to more pronounced intergrowths with well-developed

[†] Department of Microbial and Molecular Systems, Katholieke Universiteit Leuven.
[‡] Department of Chemistry, Katholieke Universiteit Leuven.
[§] BASF AG.

morphologies. In order to maximize the performance of ZSM-5 catalysts, it is important to understand the crystallographic organization within ZSM-5 crystallites, particularly regarding access to the straight or sinusoidal pores. Several microscopic techniques have been invoked to this aim. An early electron microscopic analysis of the morphology of ZSM-5 crystals by Price et al. suggested that some components within a crystallite might be rotated by 90° around a common *c*-axis.[2] In a later series of studies, the crystal's interior was studied by optical microscopy. Especially when polarized light is used, an hourglass pattern can be discerned inside some of the coffin-shaped crystals.[3,4] Based on such observations, it has been proposed that coffin-shaped MFI crystals essentially consist of two interpenetrating crystals. In this 2-component model, the crystal contains, besides a main component, two pyramidal components, the crystallographic orientation of which is rotated by 90° around the common *c*-axis (see Figure 1b). According to this view, the hourglass marks the boundaries of the 90° rotated pyramidal crystal components. There are important consequences for the accessibility of the pores: due to the changed orientation within the pyramidal components, the sinusoidal channels appear not only at the (100) faces of the crystallite but also at its hexagonal (010) facets, which are in fact the (100)′ faces of the intergrown crystal component. The 2-component model thus implies that there is hardly any access to the straight channels from the outer crystal surface.

This 2-component model has been challenged based on AFM observation of the exterior surface of individual coffin-shaped crystals.[5] Elevated terraces are observed on both the (100) and the (010) faces of coffin-shaped crystals, but the step heights are different on both faces. In rationalizing these observations, it is assumed that local symmetry anomalies arise on a growing crystal face by erroneous incorporation of a pentasil chain. However, such defects are more easily overcome in the [100] growth direction than in the [010] direction, and this ultimately leads to differences in step heights. The crystallographic orientation is the same in all parts of the crystal, but the crystal contains three pairs of components with different defect concentrations. In this 3-component model, the crystal components generate an hourglass pattern because of the different defect concentrations and resulting refractive indices, rather than by having a different orientation. Importantly, and in contrast to the 2-component model, this 3-component model implies that the straight pores can be accessed from the (010) faces.

The internal structure of coffin-shaped ZSM-5 crystals has also been studied with other approaches,[6–9] such as optical observation of I_2 adsorption,[6] interference microscopy,[7] or polarized infrared microscopy.[9] While these techniques give valuable information, *e.g.*, regarding diffusion barriers inside the crystallites or on the location and orientation of adsorbed organics in the pore system, they do not allow for unambiguous decision between the 2- and 3-component models. Fluorescence microscopy is a recent addition to the toolbox of the physical chemist studying zeolites.[10–21] We have introduced this technique to follow the catalytic oligomerization of furfuryl alcohol inside individual ZSM-5 crystals, and we have demonstrated the existence of internal diffusion barriers.[22] Shortly after, Weckhuysen and co-workers adopted a similar approach in which the local activity was probed via the formation of colored styrene oligomers. In these studies polarized light optical microspectroscopy was used to follow product formation inside ZSM-5 crystals. Many of their observations were consistent with the 2-component model.[23,24] Clearly, in all these approaches, the results will be dependent on the molecular dimensions of the selected reagents and the expected products and on their fit in the respective channel types.[9,25–27]

While the application of various techniques may result in different opinions, a second major source of disagreement is the different materials that have been used in the various reports. Comparison of the reported materials indeed reveals obvious differences in the crystal morphology, especially regarding size, aspect ratio, degree of intergrowth, etc.[2–9,22–24] In order to elucidate the internal organization of coffin-shaped MFI crystals, the present detailed study was therefore designed along the following lines: (1) In order to couple the spatial resolution of fluorescence microscopy with chemical specificity, new fluorescent probes are introduced to the study of ZSM-5 crystals

(1) Koegler, J. H.; van Bekkum, H.; Jansen, J. C. *Zeolites* **1997**, *19*, 262–269.
(2) Price, G. D.; Pluth, J. J.; Smith, J. V.; Bennett, J. M.; Patton, R. L. *J. Am. Chem. Soc.* **1982**, *104*, 5971–5977.
(3) Hay, D. G.; Jaeger, H.; Wilshier, K. G. *Zeolites* **1990**, *10*, 571–576.
(4) Weidenthaler, C.; Fischer, R. X.; Shannon, R. D.; Medenbach, O. *J. Phys. Chem.* **1994**, *98*, 12687–12694.
(5) Agger, J. R.; Hanif, N.; Cundy, C. S.; Wade, A. P.; Dennison, S.; Rawlinson, P. A.; Anderson, M. W. *J. Am. Chem. Soc.* **2003**, *125*, 830–839.
(6) Kocirik, M.; Kornatowski, J.; Masarik, V.; Novak, P.; Zikanova, A.; Maixner, J. *Microporous Mesoporous Mater.* **1998**, *23*, 295–308.
(7) Geier, O.; Vasenkov, S.; Lehmann, E.; Karger, J.; Schemmert, U.; Rakoczy, R. A.; Weitkamp, J. *J. Phys. Chem. B* **2001**, *105*, 10217–10222.
(8) Caro, J.; Noack, M.; Richtermendau, J.; Marlow, F.; Petersohn, D.; Griepentrog, M.; Kornatowski, J. *J. Phys. Chem.* **1993**, *97*, 13685–13690.
(9) Schuth, F. *J. Phys. Chem.* **1992**, *96*, 7493–7496.
(10) Roeffaers, M. B. J.; De Cremer, G.; Uji-i, H.; Muls, B.; Sels, B. F.; Jacobs, P. A.; De Schryver, F. C.; De Vos, D. E.; Hofkens, J. *Proc. Natl. Acad. Sci. U.S.A.* **2007**, *104*, 12603–12609.
(11) Roeffaers, M. B. J.; Hofkens, J.; De Cremer, G.; De Schryver, F. C.; Jacobs, P. A.; De Vos, D. E.; Sels, B. E. *Catal. Today* **2007**, *126*, 44–53.
(12) Roeffaers, M. B. J.; Sels, B. F.; Uji-i, H.; De Schryver, F. C.; Jacobs, P. A.; De Vos, D. E.; Hofkens, J. *Nature* **2006**, *439*, 572–575.
(13) Zurner, A.; Kirstein, J.; Doblinger, M.; Brauchle, C.; Bein, T. *Nature* **2007**, *450*, 705–708.
(14) Kirstein, J.; Platschek, B.; Jung, C.; Brown, R.; Bein, T.; Brauchle, C. *Nat. Mater.* **2007**, *6*, 303–310.
(15) De Cremer, G.; Antoku, Y.; Roeffaers, M. B. J.; Sliwa, M.; Van Noyen, J.; Smout, S.; Hofkens, J.; De Vos, D. E.; Sels, B. F.; Vosch, T. *Angew. Chem., Int. Ed.* **2008**, *47*, 2813–2816.
(16) Roeffaers, M. B. J.; Sels, B. F.; De Schryver, F. C.; Jacobs, P. A.; Hofkens, J.; De Vos, D. E. *Stud. Surf. Sci. Catal.* **2007**, *170*, 717–723.
(17) Seebacher, C.; Rau, J.; Deeg, F. W.; Brauchle, C.; Altmaier, S.; Jager, R.; Behrens, P. *Adv. Mater.* **2001**, *13*, 1374–1377.
(18) Seebacher, C.; Hellriegel, C.; Brauchle, C.; Ganschow, M.; Wohrle, D. *J. Phys. Chem. B* **2003**, *107*, 5445–5452.
(19) Calzaferri, G.; Huber, S.; Maas, H.; Minkowski, C. *Angew. Chem., Int. Ed.* **2003**, *42*, 3732–3758.
(20) Pauchard, M.; Huber, S.; Meallet-Renault, R.; Maas, H.; Pansu, R.; Calzaferri, G. *Angew. Chem., Int. Ed.* **2001**, *40*, 2839–2842.
(21) Hashimoto, S.; Moon, H. R.; Yoon, K. B. *Microporous Mesoporous Mater.* **2007**, *101*, 10–18.
(22) Roeffaers, M. B. J.; Sels, B. F.; Uji-i, H.; Blanpain, B.; L'Hoest, P.; Jacobs, P. A.; De Schryver, F. C.; Hofkens, J.; De Vos, D. E. *Angew. Chem., Int. Ed.* **2007**, *46*, 1706–1709.
(23) Kox, M. H. F.; Stavitski, E.; Weckhuysen, B. M. *Angew. Chem., Int. Ed.* **2007**, *46*, 3652–3655.
(24) Stavitski, E.; Kox, M. H. F.; Weckhuysen, B. M. *Chem.−Eur. J.* **2007**, *13*, 7057–7065.
(25) vanKoningsveld, H.; Jansen, J. C.; vanBekkum, H. *Acta Crystallogr., Sect. B* **1996**, *52*, 140–144.
(26) Vankoningsveld, H.; Tuinstra, F.; Vanbekkum, H.; Jansen, J. C. *Acta Crystallogr., Sect. B* **1989**, *45*, 423–431.
(27) Grahn, M.; Lobanova, A.; Holmgren, A.; Hedlund, J. *Stud. Surf. Sci. Catal.* **2007**, *170*, 724–731.

Scheme 1. Synthesis of an Asymmetrically Substituted Perylene Diimide Dye[a,b,c,d]

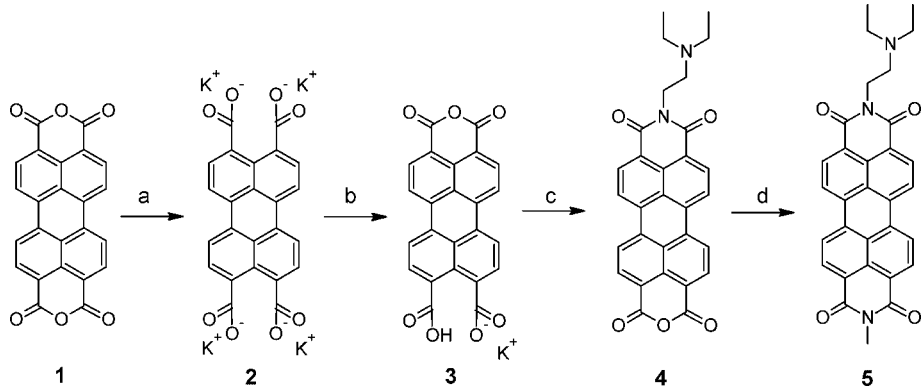

[a] KOH, 90 °C, 1 h. [b] 10 wt % H_3PO_4, drying at 80 °C. [c] 2-(*N*,*N*-Diethylamino)ethylamine, 0 °C, then 0.5 M H_2SO_4. [d] 40 wt % methylamine solution, overnight, rt.

for mapping access to straight channels and for mapping acid sites on the external surface. (2) Five batches of large ZSM-5 crystals originating from different syntheses were collected. Together, these represent the most frequently encountered morphologies of ZSM-5 crystals. (3) The samples are systematically studied not only in the fluorescence microscope but also in the SEM, AFM, and optical microscope. The combination of assays, materials, and techniques leads to a more profound insight into the origin of and relation between the commonly observed hourglass structure and the intergrowth phenomena.

Experimental Procedures

Probe synthesis. The perylene diimide dye **5** was prepared via the monoanhydride salt **3** (Scheme 1),[28] followed by further functionalization according to the approach of Tam-Chan et al.[29]

In a first step 3,4,9,10-perylenetetracarboxylic dianhydride (**1**) (0.392 g) was hydrolyzed by adding it to a solution of 0.5 g of KOH in 10 mL of water. The reaction mixture was stirred at 90 °C for 1 h, resulting in a yellow fluorescent solution of **2**. Precipitation of the monopotassium salt was induced by adding a 10 wt % H_3PO_4 solution until a pH of ~4 was reached. After a cooling period this precipitate was separated by filtration, washed with water, and dried in a desiccator at 80 °C. This resulted in 0.444 g of compound **3** which was subsequently suspended in 10 mL of water and cooled in an ice bath. Next, 2-(*N*,*N*-diethylamino)ethylamine was added in a molar ration of 3:1. This reaction mixture was stirred for 3 h; the ice bath was removed after 30 min. Afterward the suspension was acidified with 8 mL of a 0.5 M H_2SO_4 solution to yield **4** which was separated by filtration and washed with 200 mL of a 0.1 M H_2SO_4 solution.

From **4** the desired compound **5** was readily prepared by reacting 15 mg of **4** with 2.3 mL of methylamine solution (40 wt % in water) overnight at room temperature. The resulting precipitate was separated by filtration and washed thoroughly with water to remove the methylamine excess. The formation of **5** was confirmed by NMR spectroscopy. This product was used without further purification. In the following discussion compound **5** will be denoted as "PDI-TEA", according to its two main functionalities: a perylene diimide core and a triethylamine-like side chain. ^{1}H NMR ($CDCl_3$, 300 MHz): δ 8.43–8.60 (m, 8H, aromatic), 4.32 (t, 2H, J = 7.3 Hz), 3.59 (s, 3H), 2.85 (t, 2H, J = 7.3 Hz), 2.70 (q, 4H, J = 6.9 Hz), 1.12 (t, 6H, J = 6.8 Hz); MS-ESI$^+$: m/z 504 (MH^+).

Zeolites. Five ZSM-5 samples were used, with different crystal sizes, morphologies, degrees of intergrowth, and Si/Al ratios. The data are compiled in Table 1. Figure 2 shows scanning electron micrographs of individual crystals from the different batches. Sample A was prepared by a modification of the method described by Sano et al., with Si/Al = 115 in the synthesis gel.[30] Sample B was prepared according to method (III) from the paper of Müller and Unger, with as gel composition 8TPABr/123$(NH_4)_2O$/Al_2O_3/1400SiO_2/2280H_2O and with crystallization for 7 days at 180 °C.[31]

Table 1. Summary of the Different ZSM-5 Samples

	Dimensions (μm^3)[a]	Si/Al[b]	morphological features
Sample A	10 × 7 × 15	115	rounded boat
Sample B	15 × 10 × 80	700	perfectly shaped coffin
Sample C	15 × 10 × 80	40	coffin with small ramps on (010)
Sample D	7 × 5 × 25	730	coffin with central defect on (010)
Sample E	7 × 7 × 15	94	coffin with large intergrowth

[a] Approximate values along crystallographic *a*, *b*, and *c* axes determined by SEM. [b] Si/Al ratios based on the ratio in the synthesis mixture.

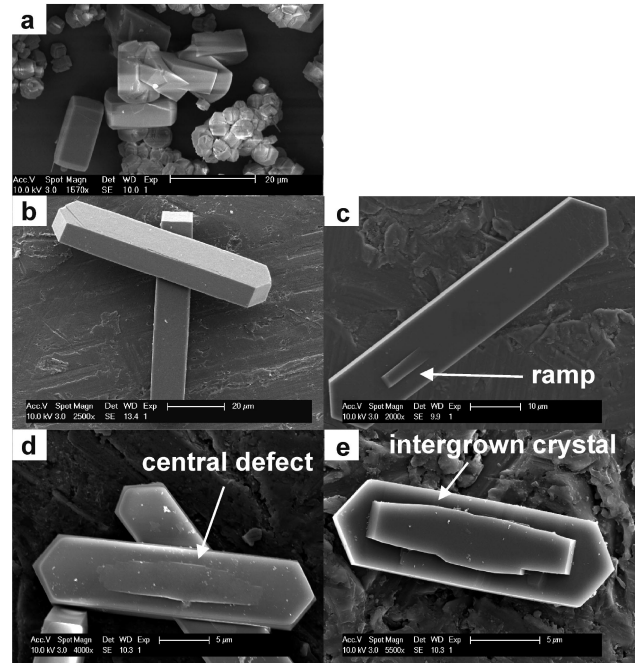

Figure 2. Scanning electron micrographs of (a) sample A (scale bar 20 μm), (b) sample B (scale bar 20 μm), (c) sample C (scale bar 10 μm), (d) sample D (scale bar 5 μm), and (e) sample E (scale bar 5 μm).

(28) Troster, H. *Dyes Pigm.* **1983**, *4*, 171–177.
(29) Tam-Chang, S. W.; Seo, W.; Iverson, I. K. *J. Org. Chem.* **2004**, *69*, 2719–2726.
(30) Sano, T.; Wakabayashi, S.; Oumi, Y.; Uozumi, T. *Microporous Mesoporous Mater.* **2001**, *46*, 67–74.

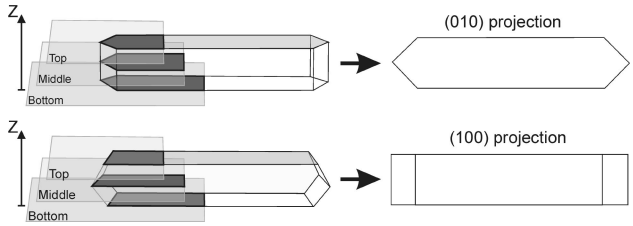

Figure 3. Projection of MFI crystals along two directions. The focal plane can be adjusted in the *Z*-direction to correspond with the bottom, middle, or top of the crystal.

Samples C and D were prepared according to methods from the same paper, respectively, using method (IV), 8TPABr/123$(NH_4)_2O$/Al_2O_3/80SiO_2/2280H_2O, and method (V), 8TPABr/123$(NH_4)_2O$/Al_2O_3/1460SiO_2/2280H_2O.[31] Sample E was prepared following a procedure described by Chen et al. with Si/Al = 94.[32]

Materials. 4-(4-Diethylaminostyryl)-*N*-methylpyridinium iodide (DAMPI), methylamine (40 wt.% in water), *N*,*N*-diethylaminoethylamine (≥98%), concentrated sulfuric acid, perylene-3,4,9,10-tetracarboxylic dianhydride (≥98%), phosphoric acid, 1,4-dioxane (anhydrous, 99,8%), *n*-butanol (spectroscopic grade), and chloroform (spectroscopic grade) were obtained from Sigma Aldrich.

Fluorescence Microscopic Assays. For the fluorescence microscopic investigations, the NH_4-exchanged zeolites were calcined under air. This procedure consisted of heating the sample with a rate of 1 K min^{-1} up to 353 K and holding this temperature for 4 h, followed by heating at 1 K min^{-1} to 393 K, keeping the sample there for 4 h and further heating at 1 K min^{-1} to 798 K, at which temperature the sample was finally held for 24 h. After cooling to room temperature the crystals were contacted with the dye solution for 24 h before spin coating the sample on a cover glass. For the DAMPI experiments a 2 mM solution in *n*-butanol was used; PDI-TEA was used as a 5 μM solution in chloroform. After spin coating the dye-loaded crystals on a glass cover slide (2000 rpm, 1 min), the cover glasses were placed in a home-built sample holder.[33] Herein the sample is sandwiched between a brass base and a Teflon holder, which contains the liquid during the measurements. A silicone rubber sealing is used between the Teflon and the glass.

A Fluoview 500 system (Olympus) was used for the confocal fluorescence microscopic studies. The fluorescence signal generated by a 488 nm Ar^+ laser (Spectra Physics) is detected using a photomultiplier tube (PMT) after passing a dichroic mirror (488 nm) and a 505 nm long pass filter. Within one sample the same detector settings and color scaling are used to make a direct comparison more straightforward. Care was taken not to oversaturate the PMT. A line profile of the fluorescence intensity along a selected line is used as a quantitative measure for the local fluorescence intensity. Samples are shown either in (010) or in (100) projection (Figure 3). As a rule, the projection shown is that of a section through the middle of a crystal, lying on either (100) or (010).

Atomic Force Microscopy (AFM). AFM measurements were performed using a Topometrix Explore AFM (Explore, Veeco/Topometrix) along with an optical microscope (IX71, Olympus). Samples were imaged in air in tapping mode with a drive frequency of 200–300 kHz using silicon nitride oxide sharpened tips (Veeco). The AFM tip was positioned exactly on the ZSM-5 crystal by observing the crystal with the optical microscope. All images were background leveled (up to second order). The crystals were spin coated on a cover glass coated with a thermopolymer. The samples were then slowly heated to ~50 °C and kept at that temperature until part of the crystals sank into the polymer layer.

Scanning Electron Microscopy (SEM). Scanning electron micrographs were recorded on Au-coated zeolite samples using a Philips XL 30 FEG microscope.

Results

Scanning Electron and Atomic Force Microscopy. First, the crystal morphology and the structure of the outer surface were described in detail for every sample using scanning electron microscopy (SEM) and atomic force microscopy (AFM). Sample A consists of well-formed rounded-boat crystals that range in size from 10 × 7 × 15 μm^3 to 12 × 10 × 20 μm^3. On the electron microscopic images the outer surfaces have a smooth appearance (Figure 2). Next to the micrometer-sized rounded-boat crystals, sample A contains smaller particles that are readily observable. These particles lack a clear morphology and are too small for further optical microscopic studies; they are not further discussed. Samples B, C, D, and E comprise crystals with the coffin-shape morphology. The sizes vary from 15 × 10 × 80 μm^3 for samples B and C to 7 × 5 × 25 μm^3 for sample D and 7 × 7 × 15 μm^3 for sample E. Detailed analysis of the SEM images in Figure 2 reveals that the different samples have characteristic sizes but also distinct defect structures which are important for further study. The morphological details are summarized in Table 1.

AFM analysis of the outer surface of these samples reveals details that are not visible on the SEM pictures. The rounded-boat crystals of sample A contain small nanometer-sized terraces radiating out from central points on the (010) and (100) faces, in line with the observation of Agger et al. (Figure 4a).[5] This surface structure is sometimes obscured by the presence of small crystallites grown on top of this same face, seen as distinct plateaus, with a similar rounded-boat morphology, and demarcated by large steps of ~100 nm high. These crystallites show similar concentric nanometer-sized steps radiating out from the center. Atomic force micrographs of the perfectly coffin-shaped crystals of sample B have been reported in our previous fluorescence microscopic study.[22] On both the (010) and the (100) faces, elevated terraces are observed; the terrace heights on the (010) face are 1 order of magnitude larger than those on the (100) face. A similar situation was described by Agger et al. for coffin-shaped crystals.[5]

On the (100) face of the coffin-shaped crystals in sample C, terrace heights are uniform at around ~5 nm . The steps at the (010) face are less uniform; the step height ranges from a few nanometers in the center to 40–100 nm at the crystal tips (Figure 4b). In the case of sample D, it proved difficult to approach the narrow (100) face by AFM, because of the flat shape of the crystals. Moreover, the defects that were observed in SEM result in the (010) surface being rather rough, and this impedes a detailed observation of an underlying step structure. Finally, sample E contains a large, central intergrowth on the (010) faces. Analysis of the step heights on the different faces supports the idea that these crystals consist of a 90° intergrowth, in agreement with the morphological characteristics (data not shown). The step heights on (010) are higher than those on (100) or on (100)′ of the intergrown component.

Fluorescence and Optical Microscopy. After the morphological characterization, the different ZSM-5 samples were subjected to fluorescence assays. As a working hypothesis, it is assumed that PDI-TEA can be used as a probe for monitoring the presence of acid sites on zeolite crystals. In the free base, the

(31) Mueller, U.; Unger, K. K. *Zeolites* **1988**, *8*, 154–156.
(32) Chen, S. Z.; Huddersman, K.; Keir, D.; Rees, L. V. C. *Zeolites* **1988**, *8*, 106–109.
(33) Roeffaers, M. B. J.; Sels, B. F.; Loos, D.; Kohl, C.; Mullen, K.; Jacobs, P. A.; Hofkens, J.; De Vos, D. E. *ChemPhysChem* **2005**, *6*, 2295–2299.

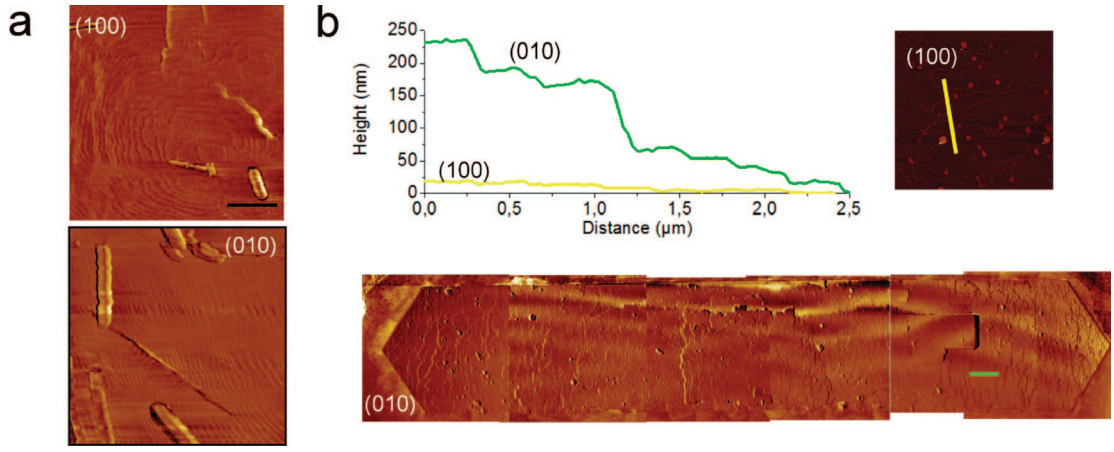

Figure 4. AFM observation of (010) and (100) faces of ZSM-5 crystals: (a) Concentric terraces present on two crystal facets of a crystal of sample A; scale bar 1 μm. (b) The step heights on two facets of a crystal from sample C. The green line is a 2.5 μm profile recorded in the tip zone of the hexagonal facet; the yellow line shows a 2.5 μm profile on (100).

tertiary amine functions efficiently quench the fluorescence of the perylene diimide chromophores through photoinduced electron transfer (PET).[34] However, when the base reacts with an acid site, the fluorescence is restored. In view of its large dimensions, it is assumed that PDI-TEA only has access to acid sites on the external surface, or at defects, if the crystals contain any. The second probe, DAMPI, will be used to image adsorption at the entrance of straight pores. DAMPI contains a stilbene-like backbone and is almost nonfluorescent in solution due to *cis*−*trans* isomerization. The chromophore's emissive properties are restored if the *cis*−*trans* isomerization is sterically prevented, for instance, by a narrow fit in a zeolite pore.[17] Previous X-ray diffraction studies by Parise et al. have shown that stilbene molecules show a strong preference for orientation along the straight channels of the MFI structure.[35] Therefore, DAMPI is assumed to selectively visualize those zones of the crystal surface that give access to the straight MFI channels. Because of the size of the diethylamino group, further intrusion of the dye into the intact 10-MR framework is unlikely. These hypotheses will be validated at the end of the Results section. A similar approach for visualizing the outer surface of growing salt crystals by chromophore adsorption has been proposed by Kahr et al., both at the single crystal and at the single molecule level.[36–39]

The distribution of PDI-TEA at the outer surface of the crystals in sample A can be evaluated by measuring the emission intensity in the two projections of Figure 5a. Clearly, the dye distribution on the crystal's outer surface is homogeneous. The line profiles show similar peak intensities for all faces. The fluorescence intensity in the solution is negligible. The crystal interior seems to be free of dye; this is also the case for all the following samples. For the DAMPI assay, the (010) projection shows homogeneous fluorescence around the crystals' periphery (Figure 5a). However the (100) projection reveals a clear accumulation of dye at the (010) crystal faces. These faces show a strongly increased fluorescence compared to the other faces. Out-of-focus fluorescence from these strongly fluorescent faces is at the origin of the slightly increased intensity visible in the crystals' interior on the (010) projection.

Figure 5b shows representative fluorescence images for sample B, containing the perfectly shaped coffin-type crystals. Using both fluorescent probes, the results for this sample are very similar to those obtained for the rounded-boat crystals: PDI-TEA is homogeneously distributed over the outer surfaces, while DAMPI is clearly accumulated at the (010) faces. In the optical transmission micrographs an hourglass structure is clearly visible even without crossed polarizers (Figure 6b); the phenomenon is essentially the same as when observed with crossed polarizers.[4,5,40]

Figure 5c shows that PDI-TEA is as well homogeneously distributed on the outside of the coffin-type crystals with small ramps in sample C. As for the previous samples, the crystals' circumference in both projections has a similarly intense emission. While this is the case for a majority of crystals, Figure 7 shows the results of sorption on an accidentally broken crystal. Remarkably, while the outer surface is strongly fluorescent, the exposed "interior" part of the crystal is unreactive.

Loading of sample C with DAMPI results in a more complex fluorescence image. In the (100) projection a strong accumulation of the dye at the extremities or tips of the hexagonal faces is visible (Figure 5c). These zones with a strong dye accumulation are even more clearly visible on the (010) projection of the bottom surface. Two zones can be discriminated: the dye seems to be less abundant in the central area, but the areas near the crystal tips display increased emission intensity. The ramps are sufficiently large to be observed in the fluorescence microscope (Figure 5c, insets). Their softly sloped top side is not colored by DAMPI. Images taken at different *Z*-positions rule out the possibility of an artifact due to restricted focus depth. The lateral faces of the ramps strongly accumulate DAMPI, as can be seen in the insets of Figure 5c. In the optical transmission images, the outer surface appears smooth with the exception of the small ramp on the hexagonal face (Figure 6c). The hourglass

(34) Daffy, L. M.; de Silva, A. P.; Gunaratne, H. Q. N.; Huber, C.; Lynch, P. L. M.; Werner, T.; Wolfbeis, O. S. *Chem.−Eur. J.* **1998**, *4*, 1810–1815.
(35) Parise, J. B.; Hriljac, J. A.; Cox, D. E.; Corbin, D. R.; Ramamurthy, V. *J. Chem. Soc., Chem. Commun.* **1993**, 226–228.
(36) Barbon, A.; Bellinazzi, M.; Benedict, J. B.; Brustolon, M.; Fleming, S. D.; Jang, S. H.; Kahr, B.; Rohl, A. L. *Angew. Chem., Int. Ed.* **2004**, *43*, 5328–5331.
(37) Claborn, K.; Puklin-Faucher, E.; Kurimoto, M.; Kaminsky, W.; Kahr, B. *J. Am. Chem. Soc.* **2003**, *125*, 14825–14831.
(38) Kahr, B.; Gurney, R. W. *Chem. Rev.* **2001**, *101*, 893–951.
(39) Wustholz, K. L.; Bott, E. D.; Isborn, C. M.; Li, X. S.; Kahr, B.; Reid, P. J. *J. Phys. Chem. C* **2007**, *111*, 9146–9156.
(40) Karwacki, L.; Stavitski, E.; Kox, M. H. F.; Kornatowski, J.; Weckhuysen, B. M. *Angew. Chem., Int. Ed.* **2007**, *46*, 7228–7231.

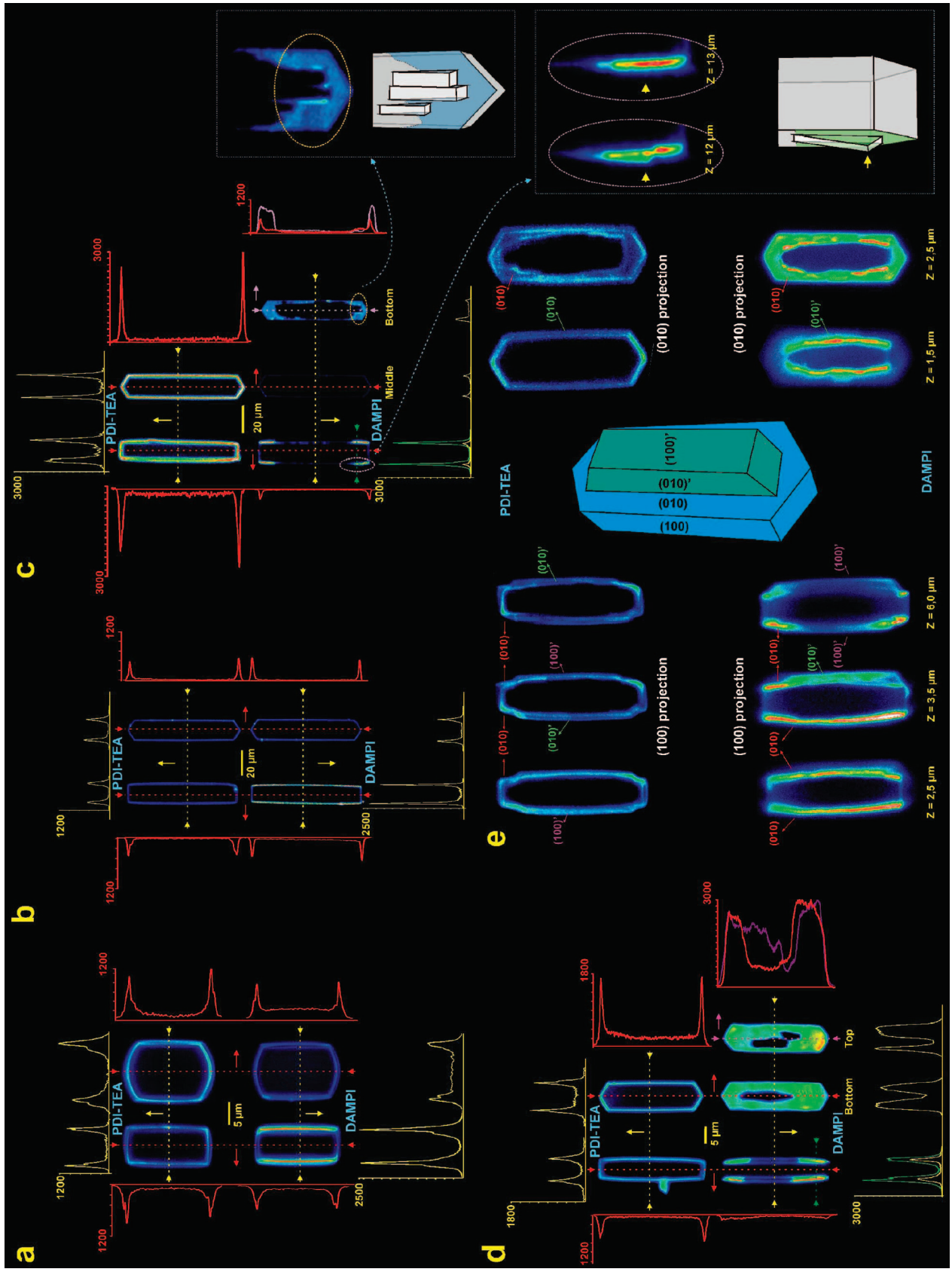

Figure 5. Fluorescence microscopic images in the false color mode for (a) sample A, (b) sample B, (c) sample C, (d) sample D, and (e) sample E. In each pane, the upper half shows PDI-TEA adsorption, and the lower half, DAMPI adsorption; (100) projections are shown at the left, and (010), at the right side. Intensity profiles along selected lines in (a−d) allow quantitative comparison of dye adsorption within each sample. For (c), the insets zoom in on the DAMPI-colored ramps on the (010) face: the top side of the ramps is not fluorescent (upper inset), while the lateral face of the ramp (at $Z = 12$ μm) is stained by DAMPI (lower inset). In (e), images are recorded at different Z-positions and crystal faces are labeled as indicated on the schematically drawn intergrown crystal.

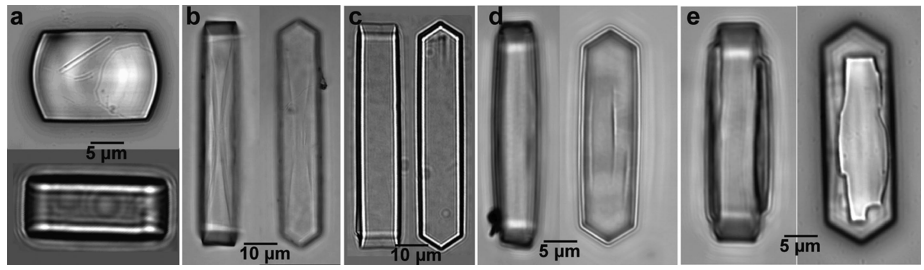

Figure 6. Optical transmission images for (a) sample A, (b) sample B, (c) sample C, (d) sample D, and (e) sample E.

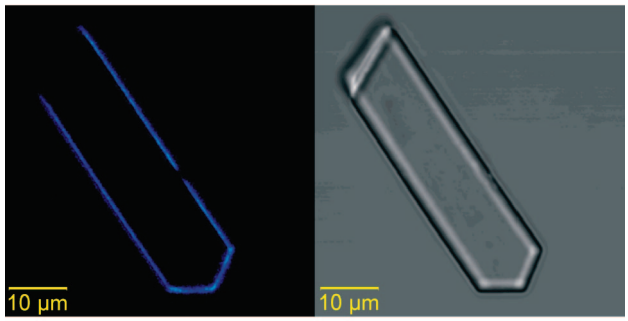

Figure 7. PDI-TEA sorption on a broken crystal: (left) fluorescence image, (right) optical image.

shaped structure can be observed in the crystal's interior; however, there is no evidence that its symmetrical contours coincide with the irregular shapes of the large central defects, observed in the fluorescence images of the macroscopic hexagonal faces.

Measurements on sample D yield comparable results as those for sample C, with a homogeneous distribution of PDI-TEA at the crystal's surface and a strong accumulation of DAMPI molecules in some zones of the hexagonal faces (Figure 5d). Comparison of the top and bottom (010) projections of the DAMPI-loaded crystals shows that the dark zones on the hexagonal faces are not symmetrically positioned at both sides of one crystal (Figure 5d). The dye-depleted zones are readily correlated with the central defect zones observed in the SEM images (Figure 2d) or in the optical transmission images (Figure 6d). Hourglass structures could not readily be observed in the optical images.

Sample E contains the crystals with the most obvious and the largest amount of defects. These defects, which look like intergrown crystals, are so large that they are also easily visible on the optical transmission images (Figure 6e). Therefore, one has to be cautious in analyzing the fluorescence images. If a specific zone remains dark, this could be due to a lack of dye adsorption but also to the limited focus depth of the confocal microscope. Artifacts can be easily overcome by varying the focal plane, as is done in the micrographs of Figure 5e. By scrolling through the *Z*-direction, it can be seen that PDI-TEA is fairly homogeneously distributed over the crystal surface. By contrast, the DAMPI molecules are very heterogeneously distributed over the outer surface. From images taken along different orientations, it is obvious that DAMPI has a clear preference for the (010) plane of the main crystal and the (010)′ plane of its large intergrowth (schematically, see Figure 5e).

Further experiments were conducted to check the structural stability of the coffin-shaped zeolite crystals. It has often been reported that 90° intergrowths can be dislodged, e.g., by ultrasonic treatment.[3] Therefore, wet crystal batches were calcined very fast (50 K min^{-1}) to 823 K in an attempt to disrupt the different crystal compounds and next exposed to the DAMPI dye. Because of the complexity of the crystals in sample E, these experiments were only performed on samples B, C, and D. No effects were seen on wet-calcined crystals from samples B and D. However, for sample C, this treatment resulted in the generation of defects that are readily visualized by the DAMPI probe as bright regions in the crystals' interior (Figure 8). The defects seem to be restricted to the crystal sections below the zones on (010) that are not stained by DAMPI.

As was indicated before, both fluorescence assays are based on working hypotheses. For PDI-TEA, it is assumed that the dye only interacts with freely accessible acid sites on the outer surface. For DAMPI, it is hypothesized that the dye is selectively adsorbed in the entrances of straight MFI channels; this implies that the DAMPI adsorption is not controlled by acid–base reactions or by ion exchange. These hypotheses were subjected to a test. In a first experiment, a crystal equilibrated with PDI-TEA is exposed to a high concentration of triethylamine (Figure 9). This results in a complete loss of fluorescence at the crystal's surface, due to competitive adsorption at the outer surface. Consecutive acidification of the solution with acetic acid reveals the presence of large amounts of the PDI-TEA in solution, which are not visible under basic conditions because of PET. Thus competition with the large excess of triethylamine prevents the specific adsorption of the dye at the crystal's surface. In another experiment the selective adsorption of DAMPI was tested. This molecule contains a quaternary ammonium group that could be responsible for cation exchange and an aniline moiety that could react with strongly acidic sites. However, the fluorescence signal of a DAMPI-loaded sample is not at all influenced by a large excess of triethylamine. Interaction of DAMPI with acid sites therefore can be ruled out. Similarly, the DAMPI images are insensitive to a 1 M aqueous $MgCl_2$ solution, which rules out that the zeolite-DAMPI interaction is based on cation exchange. Summarizing, the PDI-TEA assay is specific for freely accessible acidic sites; the DAMPI molecules are adsorbed in the pore entrances of the straight channels, without interference by acid–base or ion-exchange phenomena.

Discussion

The electron and atomic force microscopic characterizations show that sample A contains relatively small rounded-boat-shaped crystals with circular growth fronts radiating out from a limited number of nucleation points.[41] PDI-TEA adsorbs homogeneously on the crystal's exterior surface, resulting in a bright outer rim in the fluorescence sectional views. This

(41) Meza, L. I.; Anderson, M. W.; Agger, J. R.; Cundy, C. S.; Chong, C. B.; Plaisted, R. J. *J. Am. Chem. Soc.* **2007**, *129*, 15192–15201.

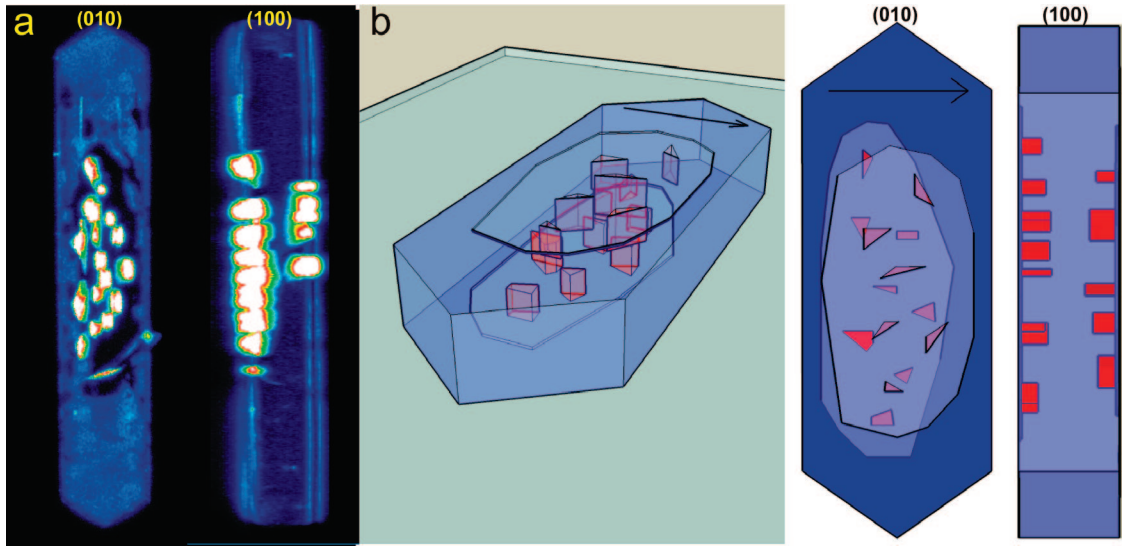

Figure 8. DAMPI adsorption on an intentionally damaged crystal of sample C. (a) Fluorescence images in the (010) and (100) projections. The images were obtained by recording an image stack at various *Z*-positions, followed by 3-D reconstruction and projection on (010) or (100). Defects are mostly formed below the central zones on (010) which are not colored by DAMPI in undamaged crystals (as in Figure 5c, bottom right). (b) Scheme clarifying the position of the defects in the crystallite.

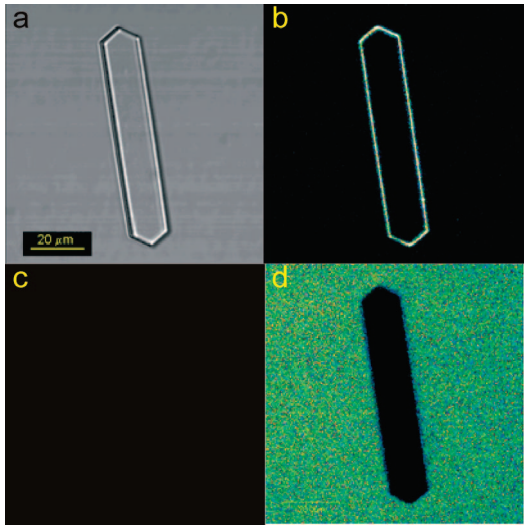

Figure 9. Validation of the PDI-TEA fluorescence assay for a crystal of sample B. (a) Optical image; (b) image after PDI-TEA staining; (c) is (b) after addition of excess Et_3N; (d) is (c) after acid addition.

indicates a homogeneous distribution of accessible acidic sites on the external surface. The measured external acidity is influenced by two factors: the local framework aluminum concentrations and the accessibility of acid sites at the outer surface. The former is determined by the time-dependent Si and Al incorporation during crystal formation, and hence the outer layer, which is formed in the final crystallization stage, should contain similar amounts of aluminum at the different crystal faces. As PDI-TEA is much larger than either pore type, it is not possible to discriminate between straight and sinusoidal pores, and the measured acid sites must be located on the outer surface or in the pore entrances.

By contrast, the DAMPI assay shows a pronounced preference toward the (010) faces of the rounded-boat crystals. For such crystals, there is a general consensus that the sinusoidal pores can be accessed from the rectangular (100) faces, while the straight pores can be entered from the large rounded (010) faces. Hence, Figure 5a proves that DAMPI selectively visualizes the entrances to the straight pores, in accordance with the known preference of stilbene structures for straight MFI channels.[35] DAMPI is thus ideally suited to discriminate between the two different pore systems at the external surface. The fact that neither of the assays' pronounced fluorescence can be detected from the crystals' interior proves that no crystal damage, e.g., mesopore formation, has been induced by the synthesis or by the consecutive activation steps, like repeated calcination or ion exchange.

The other samples B−E contain coffin-shaped crystals, with increasing defect contents in going from the perfect crystals of sample B to the strongly intergrown crystallites of sample E. All these samples show a homogeneous coloration of the external surface by PDI-TEA, reflecting the even distribution of accessible acid sites. The strong fluorescence of the outer surface, compared to the exposed interior of a broken crystal (Figure 7), is attributed to the zoning of Al-atoms in ZSM-5 crystals, causing the acid sites to be located mainly at the crystal's edges. Figure 7 also proves that silanol groups, which terminate a broken crystal, are not sufficiently acidic to detectably interact with PDI-TEA.

The DAMPI assay, which selectively visualizes access to straight pores, reveals much more detailed features for samples B−E. In the following, we try to establish relations between these DAMPI observations, the morphological features assembled in Table 1, and the observation of hourglass structures. Sample B contains the perfectly coffin-shaped crystals, without noticeable defects or intergrowths at the outer surface. The hourglass structure is prominently observable in all crystals. The DAMPI assay shows an elevated fluorescence at the (010) faces compared to the other faces. This shows that the pore orientation in the large, 80 μm long crystals is essentially the same as that in the rounded boats of sample A; there is no evidence of a 90° *c*-rotation of the pore system at any crystal face. The observations particularly for sample B thus contradict the 2-component model, which links the hourglass structure to a 90° rotation of a pyramidal crystal section and, hence, to sinusoidal pores

surfacing in a large rectangular zone on the hexagonal crystal facet (Figure 1). The case of sample B shows that an hourglass structure does not necessarily imply the presence of a 90° intergrowth.

However, for samples C and D, the DAMPI results support that 90° rotations have occurred in the crystallites, more specifically in the crystal parts under the hexagonal facets. DAMPI is heterogeneously distributed along the outer surface of these crystals; it strongly accumulates in the tip zones of the hexagonal facets, as seen in the various projections of Figures 5c and 5d. Centrally on the hexagonal facets, nonfluorescent zones are observed, which is consistent with a local 90° rotation and with the appearance of sinusoidal pores at the surface. Thus the hexagonal crystal face can be described as being composed of (010) at its extremities, with straight pores surfacing and of (100)′ in the central zone, with sinusoidal pores. Particularly for sample D, the dark central zones from fluorescence microscopy are readily identified with the central defect zones, as observed in the morphological characterization with SEM (Table 1). The top and bottom (010) projections of a representative crystal from sample D clearly show that the 90° rotated zones are not symmetrically positioned on the opposite hexagonal facets of the crystallite. It is therefore unlikely that these 90° intergrown sections have a common origin near the geometric middle of the crystallite. Furthermore the top (010) projection in Figure 5d shows two distinct 90° rotated sections, indicating that these sections must have started to grow independently from different points in space during the crystallization process. It is remarkable that such rotated zones are only observed on the (010) faces of the main crystallite.

In sample C, the central dark zones from fluorescence microscopy are not readily observed by SEM. However, the ramp-like features on the hexagonal facets can be recognized both in SEM and in fluorescence microscopy. The morphology of the small ramps strongly suggests that they are small, 90° intergrown sections with well-developed crystal faces. The dark soft-sloped facets can be identified as (100)′; the lateral faces of the ramps are (010)′ faces, where straight pores are surfacing and DAMPI strongly adsorbs. This is visible in the inset of Figure 5C.

Again, the observations for samples C and D are not fully in line with the proposed 2-component model: 90° rotated zones are indeed found, but their boundaries are irregular and do not coincide with the pyramidal sections under the hexagonal facets as suggested by this model. The fact that hourglass features are observed in sample C, but not in sample D, again throws doubt on a direct relation between the presence of an hourglass and the occurrence of 90° rotated crystal components. The intergrowths in sample E are even more prominent than in the previous samples. The DAMPI-fluorescence assay again visualizes access to straight pores, both on (010) of the principal crystal components and on (010)′ faces of intergrown crystals. A schematic representation is shown in Figure 5e.

Based on these data, it is possible to propose a rationalization containing elements from both previously proposed 2- and 3-component models. We have provided new evidence that MFI zeolites can exist as coffin-shaped crystals without any 90° intergrowth. Examples are the crystals from sample B in this study, and the crystals used by Agger et al. in their AFM work.[5] As crystals from both batches contain clear hourglass patterns, one can no longer sustain that the hourglass pattern arises from a 90° intergrowth. A more likely origin for the hourglass could be the varying chemical composition, especially regarding silanol concentration, of the growing crystal components from the 3-component model.

Nevertheless, in other crystal batches (C−E), there clearly are 90° intergrown sections, even if these are sometimes small, and they only partially fill the pyramidal sections of the 2-component model. We have shown that these 90° intergrown sections are only observed at the (010) faces, proving that they exclusively originate from the crystal component below (010). This raises the question as to why this crystal component is much more susceptible to 90° intergrowth. A sound answer can be found in the 3-component model, which states that the incidence of anomalous incorporation of pentasil chains is much higher in the component below (010) than in the other components. Specifically, for growth in the [010] direction, it is much more difficult to overcome such defects than for growth in the [100] direction. These differences result in terrace heights, as mapped out by AFM, being much larger on (010) than on (100), and in this respect, our results are in complete agreement with those of earlier AFM work on silicalite. It can be reasoned that there is a relation between the high defect concentration in the segment under (010) and the nucleation of 90° intergrown crystal sections. The defect incorporation on the (010) face indeed results in a temporary cessation of crystal growth, and during such a pause, nucleation of a 90° intergrown section may be initiated, even if the precise mechanism cannot be elucidated based on our data. After this nucleation, the newly developed crystal section seems to grow at least as fast as the surrounding area, resulting in patches of (100)′ on the (010) face of the mother crystal. Depending on the position and time of formation, and the relative growth rates, the 90° rotated section can overgrow the surrounding crystal face, resulting in clearly observable central defects, as in sample D, or even in clearly recognizable intergrown crystals, as observed in sample E.

At least for crystals of sample C, it could be demonstrated that the presence of 90° intergrown sections under the hexagonal facets induces structural weakness. After severe hydrothermal treatment, DAMPI is able to penetrate inside the crystallite, but only in the sections under the central zone of (010), where the sinusoidal pores surface and the 90° rotated sections are located (Figure 8). A similar approach to visualizing mesoporosity has been adopted by Seebacher et al., using the same DAMPI molecules.[17]

Conclusion

In this paper surface specific fluorescent probes have been used to stain zeolite crystals. PDI-TEA is a reliable probe for external surface acidity; DAMPI selectively visualizes the straight pores of ZSM-5 crystallites. In view of the size of both probes, the fact that they do not penetrate into properly pretreated crystals proves that there are no mesopores intruding into the crystallites.

Careful comparison of our fluorescence microscopic data with AFM, SEM, and optical data rather supports the 3-component model rather than the 2-component model, and this has important implications for the accessibility of the straight pores in ZSM-5. Nevertheless, 90° rotated zones were detected in some ZSM-5 crystallites, but in a less ordered fashion than implied in the 2-component model. The fact that the 90° intergrown sections are located under the (010) face of the mother crystal suggests that the initiation of 90° intergrowth is related to the high defect concentration in the crystal component below the hexagonal faces. In this context, and taking into account the diversity of crystal morphologies that were studied

in this and previous studies, it seems that the major points of conflict between the 2-component and the 3-component models have been resolved by the new insights provided by fluorescence microscopy. Even if at present fluorescence microscopy is most useful for relatively large zeolite crystals, it is expected that its application to other zeolite types will help in solving many other questions related to the internal structure and pore accessibility of zeolite crystallites.

Acknowledgment. M.B.J.R. thanks the Institute for the Promotion of Innovation through Science and Technology in Flanders (IWT-Vlaanderen) for a fellowship. R.A. and G.D.C. thank FWO (Research Foundation Flanders) for financial support. This work was performed within the framework of the IAP-V-03 programme "Supramolecular Chemistry and Catalysis" of the Belgian Federal government and of GOA sponsoring. We also gratefully acknowledge support from the K.U. Leuven in the frame of the Centre of Excellence CECAT.

JA7113147